Ozawa *et al. Earth, Planets and Space* (2016) 68:186
DOI 10.1186/s40623-016-0563-5

Earth, Planets and Space

FULL PAPER

Open Access

Crustal deformation associated with the 2016 Kumamoto Earthquake and its effect on the magma system of Aso volcano

Taku Ozawa*, Eisuke Fujita and Hideki Ueda

Abstract

An M_{JMA}6.5 earthquake (foreshock) and M_{JMA}7.3 earthquake (mainshock) struck Kumamoto Prefecture on April 14, 2016, and April 16, 2016. To evaluate the effect of crustal deformation due to the earthquake on the Aso magma system, we detected crustal deformation using InSAR and GNSS. From InSAR analysis, we detected large crustal deformations along the Hinagu Fault, the Futagawa Fault, and the northeast extension of the latter fault. It extended to more than 50 km, and the maximum slant-range change exceeded 1 m. Although the obtained crustal deformation was approximately explained by the right-lateral strike-slip on the fault, its details could not be explained by such simple faulting. Additionally, we found complex surface deformation west of the Aso caldera rim, suggesting that shallow fault slips occurred in many known and unknown faults associated with the earthquake. Most of the crustal deformation could be reasonably explained by four rectangle faults located along the Futagawa Fault, in the northeast extension of the Futagawa Fault, alongside the Hinagu Fault, and in the eastern part of the Futagawa Fault. The first three of faults have high dip angles and right-lateral slip. The other was a fault with a low dip angle that branched from the shallow depth of the fault along the Futagawa Fault. The normal-dip right-lateral slip was estimated for this segment. Based on the estimated fault model, we calculated the displacement and stress field around the Aso volcano by the finite-element method (FEM) to evaluate the effects on the Aso magma system. In this calculation, we assumed a spherical soft medium located at a 6-km depth beneath the area south of the Kusasenri region as the magma system and considered only static effects. The result shows complex distributions of displacements and stresses, but we can notice the following significant points. (1) The spherical magma system deformed to an ellipsoid, and the total volume was slightly increased, less than 1%. (2) The differential stress around the upper portion of the magma system was as large as 3.5 MPa. This is strong enough to open pre-existing cracks and can cause the migration of magma.

Keywords: Kumamoto Earthquake, Aso volcano, crustal deformation, InSAR, GNSS, fault model, effect on magma system

Introduction

A shallow M_{JMA}6.5 earthquake struck Kumamoto Prefecture, located in Kyushu district, southwest Japan, on April 14, 2016, at 21:26 JST. According to the Japan Meteorological Agency (JMA), the location of the hypocenter was 32.742°N, 130.809°E, at 11.4 km depth (Fig. 1). The broadband seismograph network operated by the National Research Institute for Earth Science and Disaster Resilience (NIED), called F-net (Okada et al. 2004), determined the focal mechanism as strike-slip with a north–south tension axis. A shallow M_{JMA}7.3 earthquake followed this earthquake 28 h later (April 16 1:25 JST). Its hypocenter was at 32.755°N, 130.763°E, 12.4 km depth, according to the JMA catalog (Fig. 1). F-net determined a similar focal mechanism to that of the April 14 earthquake. JMA defined these earthquakes as the foreshock and the mainshock in this seismic activity. These hypocenters were located near the junction of the Futagawa Fault and the Hinagu Fault, and aftershocks were

*Correspondence: taku@bosai.go.jp
Volcano Disaster Resilience Research Division, National Research Institute for Earth Science and Disaster Resilience, 3-1 Tennodai, Tsukuba, Ibaraki 305-006, Japan

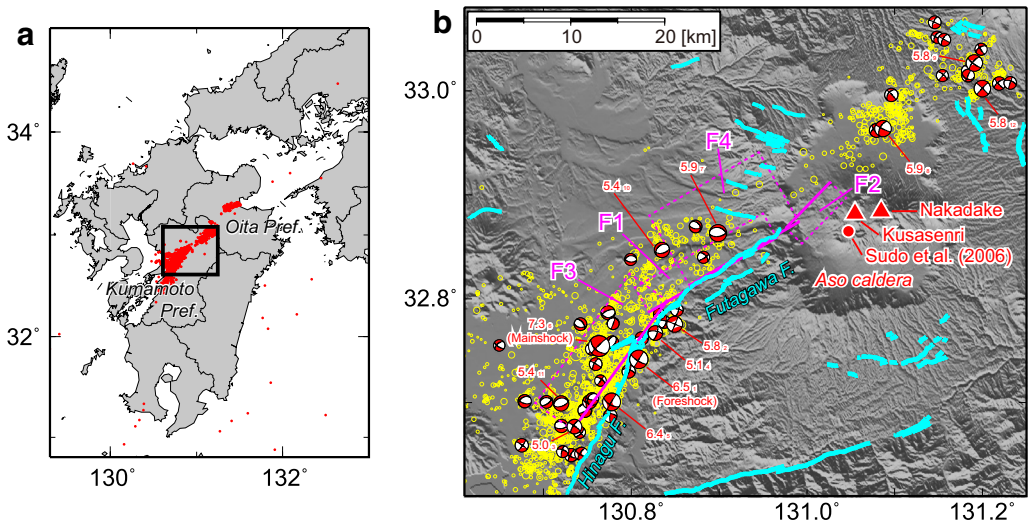

Fig. 1 **a** Map of the Kyushu district. *Red dots* indicate epicenters of earthquakes that occurred during April 14 and April 30, 2016. **b** Topographic relief map of the seismic area for the 2016 Kumamoto Earthquake. *Yellow circles* indicate epicenters of earthquakes that occurred during April 14 and April 30, 2016. Depicted focal mechanisms are shown about earthquakes with magnitude exceeding M_{JMA}4.0. An index number attached to an earthquake magnitude corresponds to an earthquake shown in Fig. 3. *Light blue curves* indicate active faults cataloged in the digital map of active faults (Nakata and Imaizumi, 2002). *Purple dashed boxes* show the fault segments estimated in this study, and *thick lines* on their boxes indicate their upper margins. *Red triangles* indicate locations of the Nakadake crater and the Kusasenri. *Red circle* indicates the location of deformation source by Sudo et al. (2006)

distributed along these faults. It has been suggested that the main rupture occurred on these faults. Looking at the hypocenter distribution in perspective, it extends to the northeast direction and reaches to Oita Prefecture, crossing the Kyushu district (Fig. 1). In that seismic zone, we found two areas where the aftershock was inactive, corresponding to the Aso and the Kuju volcanoes. In particular, the Aso volcano is located near the east end of the Futagawa Fault, and therefore a large deformation may have occurred around there.

Aso volcano has a large caldera with a size of 25 km from north to south and 18 km from east to west, and its central cones are aligned east–west in the center of the caldera (e.g., Ono and Watanabe 1985). The most violent eruption occurred about 90,000 years ago (VEI 7), and the caldera was formed in this eruption (Aso-4) (Matsumoto 1996; Aoki 2008). Nakadake, which is a central cone, is an active volcano where eruptions have occurred frequently. NIED operates a volcano observation network named V-net in several Japanese volcanoes, including the Aso volcano (Ueda et al. 2013). High activity of volcanic tremor has been observed before the Kumamoto Earthquake, but further activation or inactivation has not been observed at present (September 2016). However, the relationship between a large earthquake and volcanic activity has been discussed in many previous studies (e.g., Bautisa et al. 1996; Manga and Broadsky 2006; Lara et al. 2004; Walter 2007; Walter and Amelung 2007; Ebmeier et al. 2016). One of possible triggering mechanisms is deformation of magma system due to the earthquake. Since seismic area is close to the Aso volcano, there is a possibility that the magma system has been deformed significantly. Such deformation may cause further activation of volcanic activity in the future. Therefore, it is important to estimate how much influence the earthquake had on the Aso magma system.

In this paper, we detected crustal deformation associated with the 2016 Kumamoto Earthquake using synthetic aperture radar interferometry (InSAR) and a GNSS analysis and estimated a fault model from the obtained crustal deformations. Based on the estimated fault model, we evaluated the effect of the earthquake on the Aso magma system.

Detection of crustal deformation

InSAR analysis

After the earthquake, the Japan Aerospace Exploration Agency (JAXA) carried out frequent observations around the seismic area using the Phased Array type L-band Synthetic Aperture Radar 2 (PALSAR-2) on the Advanced Land Observing Satellite 2 (ALOS-2). We applied InSAR to SAR pairs observed before and after the earthquake and detected crustal deformation associated with the earthquake. The analyzed InSAR pairs are listed in Table 1. In this analysis, we used InSAR software called RINC (Radar INterferometry Calculation

Table 1 SAR data pairs analyzed in this study

No.	Path	Observation dates	Obs. mode	Asc/ Dsc	Look direction	Cross track	Incidence angle*
1	23	2016/3/7–2016/4/18	SM1	D	Right	N80°W	36°
2	29	2015/1/14–2016/4/20	SM1	D	Left	N106°E	43°
3	124	2016/3/7–2016/4/19	WD1	A	Left	N105°W	39°
4	130	2015/12/3–2016/4/21	SM2	A	Right	N80°E	34°
5	132	2015/5/17–2016/4/17	SM1	A	Right	N81°E	51°
6	135	2016/3/7–2016/4/18	WD2	A	Right	N84°E	68°

* An incidence angle for SM1/2 data is about the scene center, and that for WD1 is about the Nakadake crater

tools). RINC was developed for our research on InSAR analysis and can analyze ALOS/PALSAR and ALOS-2/PALSAR-2 data. The number of looks in the interferogram generation was determined so that the ground range spacing was almost 10 m, corresponding to that of the digital terrain model (DTM) used in this analysis. This DTM was ellipsoidal height data generated from a 10-m-mesh digital elevation model published by the Geospatial Information Authority of Japan (GSI) and the EGM96 geoid model (Lemoine et al. 1997). To reduce the atmospheric delay noise, we used a method for calculating the atmospheric delay based on the JMA results for a Meso-Scale Model, the 10-km-mesh numerical weather model (Ozawa and Shimizu 2010). This method calculates atmospheric delay and radar propagation path from atmospheric pressure, temperature, and humidity using ray-tracing method. Additionally, we tuned satellite orbit so that phase of far area from seismic became negligible. Final InSAR results were geocoded with pixel spacing of 2 and 4 s (approximately 50 and 100 m) for the stripmap and ScanSAR modes, respectively.

Figure 2 is an interferogram which was generated from InSAR pair 1, which is listed in Table 1 (all interferograms appear in Additional file 1). The mainshock, the foreshocks, and several moderate-size earthquakes occurred among the observations of these InSAR pairs (Fig. 3), and therefore these interferograms show crustal deformations due to their earthquakes. A decorrelation line was identified along the Futagawa Fault (Fig. 2d). The large slant-range change detected around these areas must have been due to large deformation. A steep gradient line for the slant-range change was obtained near the Hinagu Fault (Fig. 2a, c). These decorrelation and steep gradient lines must correspond to the upper margins of faults or intersection lines of a fault extension and the land surface. The steep gradient line parallel to the Hinagu Fault is not consistent with the active fault trace, and then it may indicate that the blind fault or the spray fault have been ruptured in this earthquake. Such decorrelation and steep gradient lines were also obtained in the northeast extension of the Futagawa Fault (Fig. 2e), but its spatial distribution was complex. Many slope failures occurred around this area associated with this earthquake, and they must have caused decorrelation. Additionally, abundant groundwater in Aso caldera might be related to this complex subsidence field.

The result from InSAR pair 3, which was acquired by the west-looking mode, shows slant-range shortening in the northwest of faults and slant-range extension in the southeast (Fig. 4). In contrast, results from InSAR pairs acquired by the east-looking mode show an opposite slant-range change. Such slant-range change distributions are approximately explained by right-lateral slip of the faults, but their details cannot be explained by such simple faulting. In particular, we obtained slant-range extensions on both sides of the fault around the eastern part of the Futagawa Fault from InSAR pair 1. It is difficult to explain such crustal deformation by slip on the rectangle fault with an upper margin that corresponds to the Futagawa Fault. Therefore, another fault plane should be considered for explaining such crustal deformation.

A complex fringe pattern was obtained west of the caldera rim, suggesting that many surface deformation gaps appeared in this approximately 10 km × 10 km area (Fig. 2b). According to explanation of GSI's 10-m-mesh digital elevation model, its height accuracy is 5 m. On the other hand, perpendicular baselines for all InSAR pairs were less than 200 m. Height change corresponding to 5-m height error is less than 2 mm. Then phase gaps must have not been due to DTM error. Layover and shadow distortions were not found along these phase gaps. Furthermore, phase gaps were detected in all InSAR pairs that include this area (Additional file 1). From their facts, obtained phase gaps must be actual surface deformations not noises. To identify its features, we calculated the phase gradient indicating the gradient of the slant-range change using the method of Sandwell and Price (1998) and found many lineaments with high gradients around this area (Fig. 5). A digital map of the

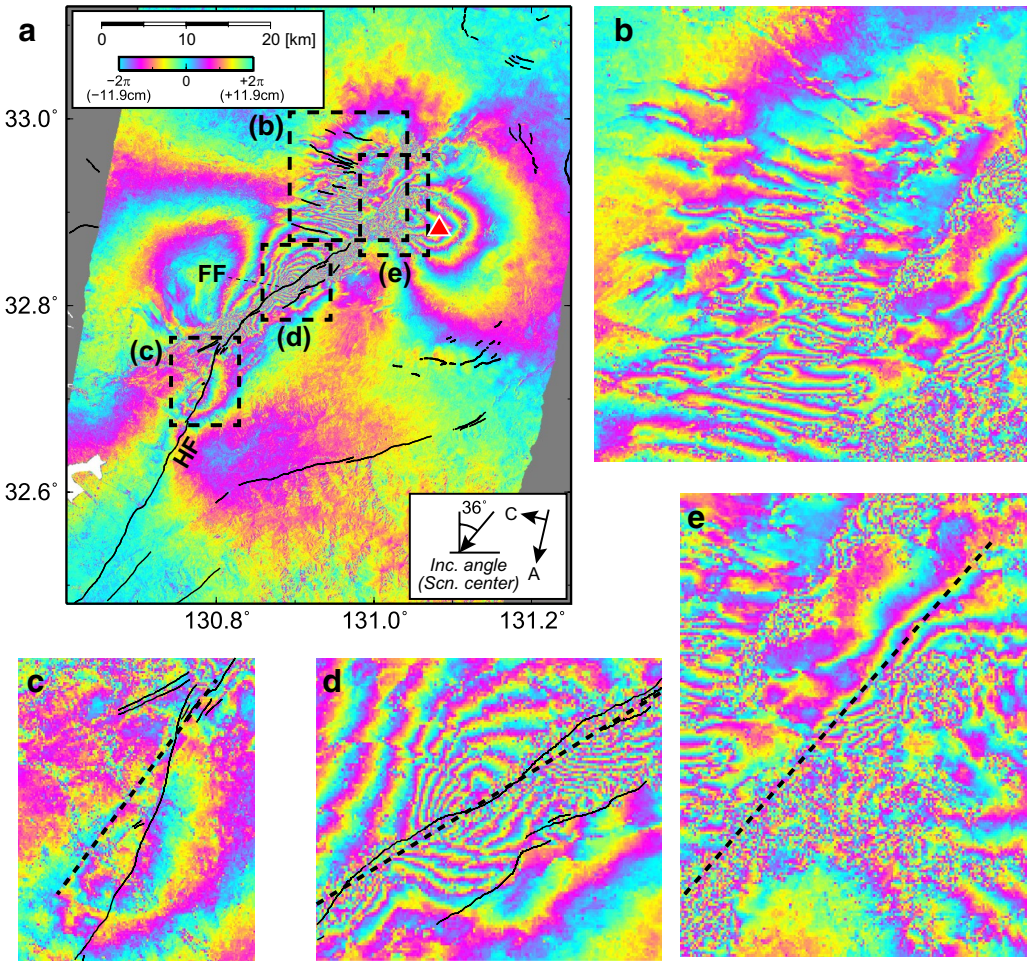

Fig. 2 **a** Interferogram obtained from InSAR pair 1 as specified in Table 1. *Color* shows wrapped phase difference between 0 and +2π radian. Phase difference of 2π radian corresponds to slant-range change of 11.9 cm. *Thin curves* show active faults cataloged in the digital map of active faults (Nakata and Imaizumi 2002). *Dashed boxes* correspond to areas shown in (**b**)–(**e**). HF and FF mean the Hinagu Fault and the Futagawa Fault. The *red triangle* indicates the location of the Nakadake crater. **b**–**e** Enlarged interferograms. *Dashed thick lines* indicate decorrelation lines or steep gradient lines of slant-range change

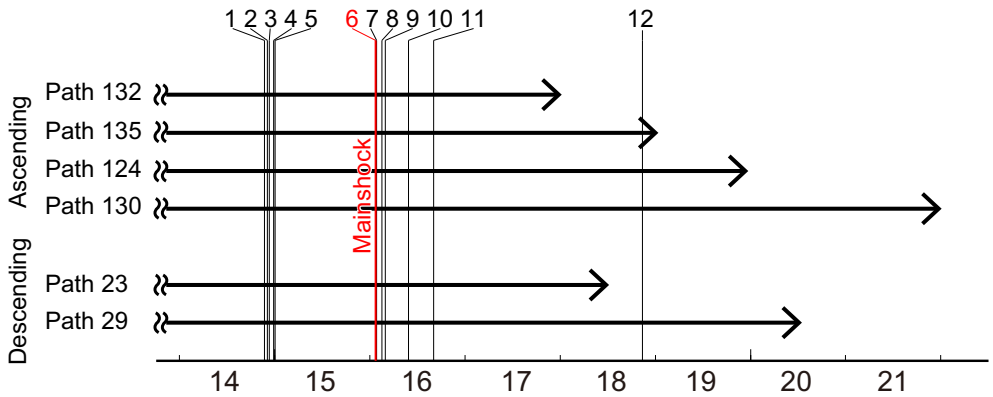

Fig. 3 Time line of the SAR data acquisition dates. A *vertical line* shows an occurence date of a typical earthquake, and a number attached to a *vertical line* corresponds to that of an earthquake shown in Fig. 1. The *red line* indicates the mainshock

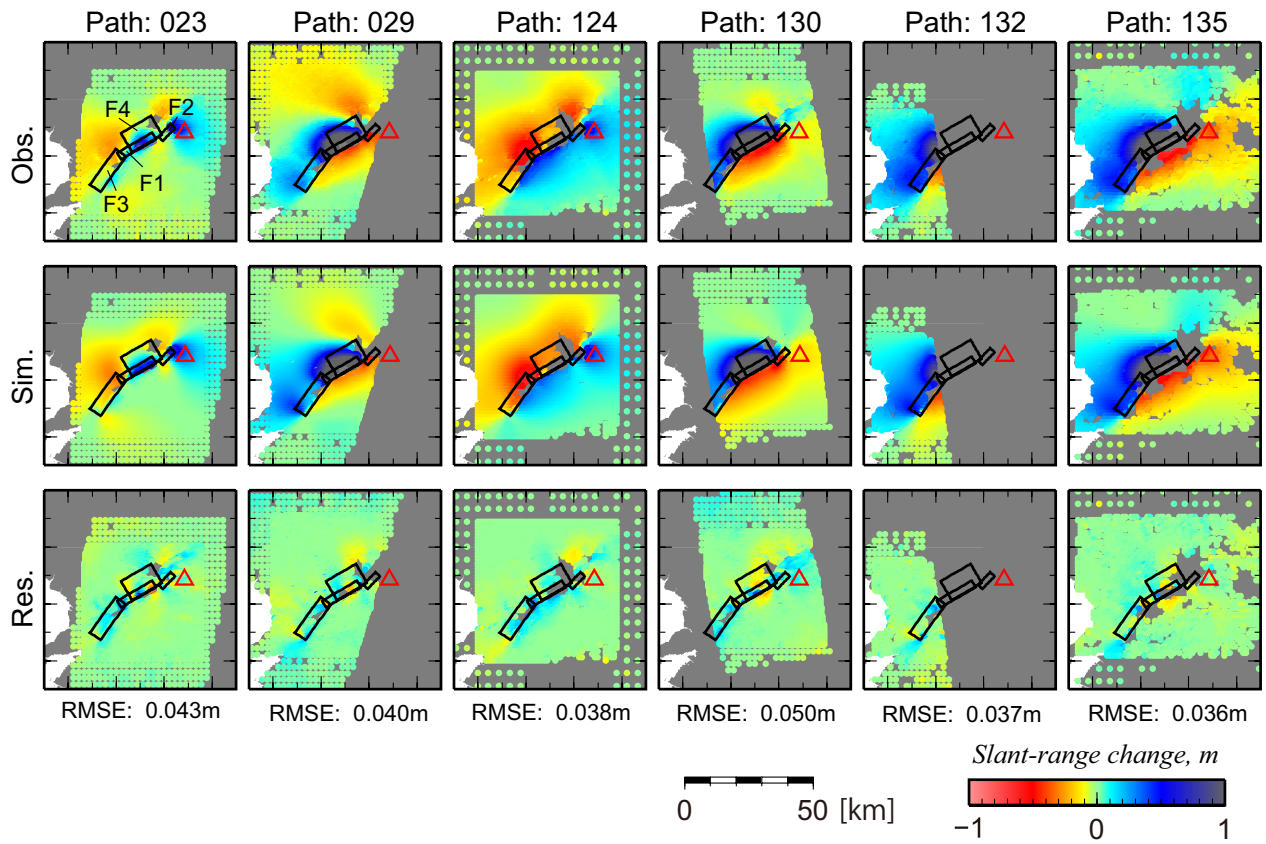

Fig. 4 Obtained slant-range change distributions and comparisons to simulated slant-range change distributions. Figures in upper (middle) *rows* represent observed (simulated) slant-range changes. Figures in the *bottom row* represent their residuals. *Solid boxes* indicate the fault segments estimated in this study. The *red triangle* indicates the location of the Nakadake crater. Root-mean-square error (RMSE) for each InSAR result is shown below the image of residual

active fault indicates that several faults are located in this area (Nakata and Imaizumi 2002), and a high phase gradient was obtained along the faults. Thus, we suppose that this complex fringe pattern indicates slips on the faults. Additionally, many lineaments with high phase gradients were also seen in areas where a fault was not shown on the map. We think that unknown faults exist in this area and that slips have occurred on the faults associated with the earthquake. It seems that the deformation has not extended over a broad area, indicating that such fault slip must have been limited to a shallow depth. This area is apart from the Nakadake, and therefore, crustal deformation due to dislocation of their faults must be negligible around the Aso magma system.

GNSS analysis

To detect crustal deformation due to the earthquake, we also analyzed GNSS data observed at 13 sites associated with V-net of NIED and GEONET of GSI. In this analysis, we used GAMIT/GLOBK software version 10.4 developed by the Massachusetts Institute of Technology with precise IGS ephemeris information. A displacement vector was estimated from the difference between the averaged coordinates in March 2016 and those during April 16 and 30, assuming GEONET site 950482, which is located more than 100 km south of the Aso volcano, to be the fixed site. Therefore, the estimated displacements include crustal deformations associated with foreshocks, the mainshock, and several aftershocks. The result generally indicated that GNSS sites located south of the fault moved to the west and that those located to north of the fault moved to the east or north (Fig. 6). In particular, an 80-cm displacement to the east-northeast was observed at GEONET site 950465, located in Kumamoto City, and a 1-m displacement to the southwest was observed at GEONET site 960701, located in the Aso caldera. 2–3-cm displacements during April 16 and April 22 were observed at their GEONET sites. Such postseismic displacements are less than 10% of coseismic displacement.

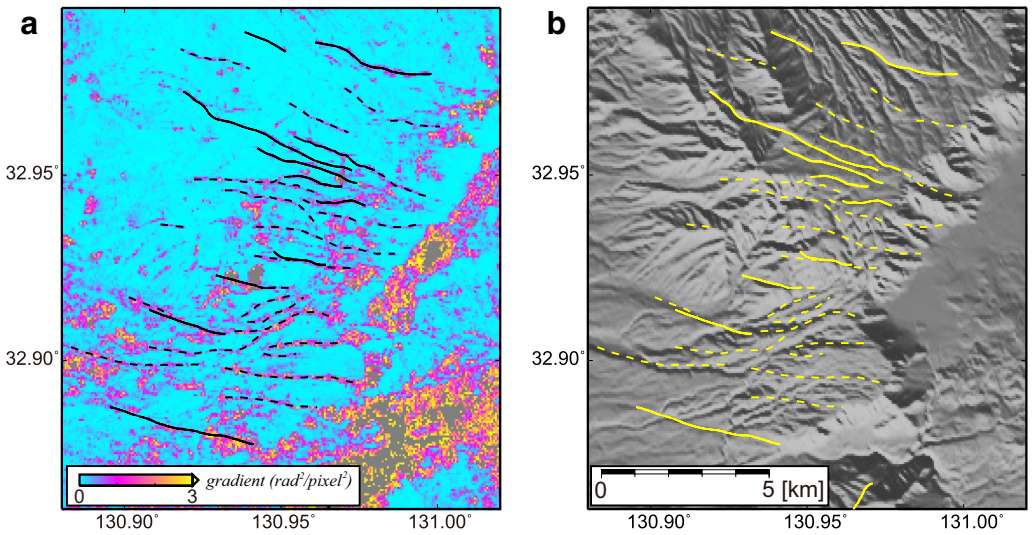

Fig. 5 **a** Phase gradient map calculated from interferogram of InSAR pair 1. Solid curves indicate active faults cataloged in the digital map of active faults (Nakata and Imaizumi, 2002). *Dashed curves* indicate lineaments with high phase gradients identified in areas where an active fault has not been cataloged. *Gray color* shows low coherence area due to large deformation. **b** Locations of lineaments with high phase gradients superposed on topographic relief map

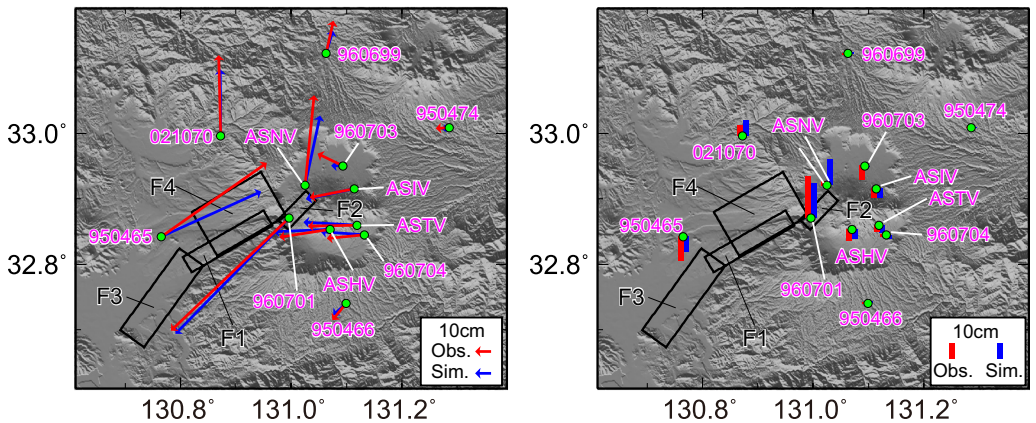

Fig. 6 Crustal displacement associated with the 2016 Kumamoto Earthquake obtained from GNSS analysis. *Red* (*blue*) *arrows* indicate observed (simulated) displacements. Fixed site is the 950482 GEONET site, located more than 100 km south of the Aso volcano. *Solid boxes* indicate the fault segments estimated in this study

Then, we assume its contribution to be negligible. At GNSS sites close to central cones, several 10-cm displacements to the west and 2–7-cm subsidence were observed, excluding ASNV close to the fault of this earthquake identified from InSAR results. These displacements approximately correspond to crustal deformation due to right-lateral slip of a fault.

Estimation of the fault model

We estimated fault models for this earthquake from InSAR and GNSS results. In this estimation, we used theoretical crustal deformation due to dislocation of a rectangular fault in an elastic half-space (Okada 1985) and estimated fault parameters that well explained the observed crustal deformations. Since the number of InSAR data exceeds 5 million, using all InSAR data in this estimation is inefficient. For efficiency of estimation, the slant-range change, based on the stripmap mode data, was picked up every 20 s (approximately 500 m) in areas where a large change was observed and every 80 s (approximately 2 km) in other areas. Slant-range changes from the ScanSAR mode were picked up

every 40 s (approximately 1 km) in areas where a large change was observed and every 160 s (approximately 4 km) in other areas. 24,306 slant-range changes from InSAR and three components of the GNSS displacement vectors for 13 sites were used in this estimation. We set a 100-fold weight on GNSS displacements relative to the InSAR slant-range change. In this fault model estimation, we considered four fault segments (F1–F4) that were suggested from interferograms. The F1 segment is along the Futagawa Fault, and the F2 segment is the northeast extension part from its east end. The F3 segment is located alongside the Hinagu Fault. The F4 segment is located alongside the F1 segment. Since the strike directions for the F1 and F3 segments could be identified clearly from interferograms, we fixed them to N240°E (F1) and N216°E (F3). Furthermore, the decorrelation line along the Futagawa Fault and the steep gradient line along the Hinagu Fault correspond to the upper margins of faults or the intersection line of a fault extension and land surface, and we constrained the fault locations so that a fault extension was consistent with that. Although the decorrelation line and steep gradient of the slant-range change were also seen around the F2 segment, we did not constrain the location of the F2 segment because the distribution might be distorted by local deformation as mentioned in the previous chapter. We then estimated all parameters for the F2 segment. Concerning the F4 segment, we assumed its strike direction to be the same as that of the F1 segment. In the fault model estimation, we first searched the presumed parameters for fault locations, sizes, dips, and strike by the trial-and-error method, and then improved the solution using the Levenberg–Marquardt (LM) method (Marquardt 1963). Generally, a non-deformation component with a long wavelength due to orbital errors and ionospheric effect remains in an InSAR result. We assumed their components to be a uniformly inclined plane and estimated them (three components for each InSAR result) with fault parameters simultaneously. Slip vectors for the four segments and non-deformation components for the six interferograms were estimated in each iteration using the linear least-square method.

The estimated fault model is presented in Fig. 7, Table 2, and comparisons between the observed and the calculated crustal deformation for InSAR and GNSS are presented in Figs. 4 and 6, respectively. Root-mean-square errors (RMSEs) for each InSAR pair were 3.6–5.0 cm (Fig. 4), and RMSE for the whole inputted data was 4.4 cm. Thus, the estimated fault model reasonably explains the observed crustal deformation. Right-lateral fault slip was estimated in the F1–F3 fault segments, corresponding to the F-net focal mechanism of the mainshock. In contrast, the slip vector for the F4 fault segment included a large normal dip-slip component. The amount of slip was estimated to be 1.8–3.6 m, and the moment magnitude was estimated at Mw7.0. The dip directions for the F1, F3, and F4 fault segments were estimated as being to the northwest, while only that for the F2 fault segment was estimated to be in the opposite direction, to the southeast. The F2 fault segment was estimated in the Aso caldera, and it dips toward the center of the caldera.

As revealed in our previous study (Ozawa and Fujita 2013) and other studies (Takada and Fukushima 2013; Pritchard et al. 2013), local deformation associated with large earthquake was detected around volcanoes. We expected that such deformation might have found above the magma chamber in residual distributions, but such local deformation was not detected in this analysis (Fig. 4). We suspect that its reason is related to the size of the affected magma chamber. In the case that the size of magma chamber is small, surface deformation due to deformation of the magma chamber is small. Provably, larger magma chamber will exist in deeper area. However, rupture in this earthquake occurred in shallow depth and typical fault dislocation was lateral slip. Therefore, crustal deformation around the deep large magma chamber must have been small. From this reason, we suspect that crustal deformation due to deformation of the magma chamber might have not been detected.

Discussion

Effect of crustal deformation on the magma system

In this section, we model the crustal structure and magma system using the finite-element method (FEM) and calculate the displacement and stress fields caused by the earthquake. The target area was set to 130.5°E–131.5°E, 32.5°N–33.3°N, and 0–40 km, and was divided into 112 × 112 × 50 elements. In addition, we re-mesh Aso volcanic area of 0.04° latitude × 0.09° longitude × 15 km depth to 112 × 112 × 50 meshes for more detailed analysis. In the elements generation for the FEM analysis, we considered topography by using a digital elevation model published by GSI. Elastic parameters at each element were derived based on Vp and Vs structures estimated by seismic tomography (Matsubara et al. 2008). We estimated the density via an empirical equation; the elastic moduli and Poisson ratios can then be obtained (Birch 1961). For a magma system, we assumed a spherical structure filled with the soft elastic; the bulk modulus was 10 GPa, and the Poisson ratio was 0.49. Sudo and Kong (2001) applied seismic tomography and detected a low velocity region about 6 km beneath an area south of the Kusasenri region. A leveling survey suggested a deflation source around the same area (Sudo et al. 2006). Considering their results, we placed a spherical soft structure with a 1-km radius 6 km deep beneath the area south of

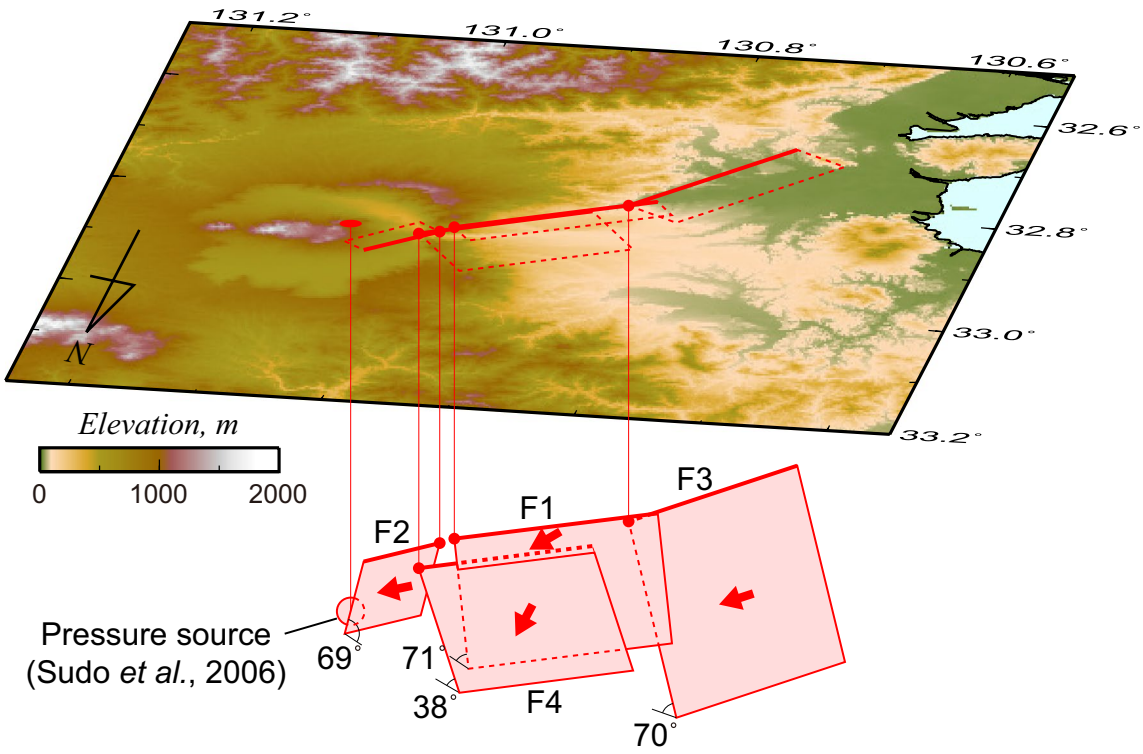

Fig. 7 Configuration of fault segments estimated in this study. The depicted pressure source was estimated by Sudo et al. (2006)

Table 2 Parameters for the estimated fault model

Segment	Lat.	Lon.	Dep.	Length	Width	Strike	Dip	Slip	Rake
	(°N)	(°E)	(km)	(km)	(km)		(deg.)	(m)	(deg.)
F1	32.859	130.966	0.0	15.8	9.2	N240°E*	71	2.65	203
F2	32.868	130.976	0.0	6.8	6.7	N44°E	69	3.64	177
F3	32.798	130.841	0.4	17.1	14.6	N216°E*	70	1.82	180
F4	32.874	130.991	1.8	13.5	10.9	N240°E*	38	1.95	235

* Strike directions were fixed to those read from the interferograms

the Kusasenri region. To remove the artificial reflection from the finite boundaries, we applied "infinite elements" at the horizontal and bottom boundaries. Applying slips on the four fault segments estimated in this study, we calculated the displacement and stress fields around the Aso magma system.

Figure 8 presents perspective views of the estimated displacement distributions on the surface of the magma system from southwest and northeast. Fault dislocation with right-lateral slip drags the magma system to the southwest, and then the upper hemisphere is moved approximately 43 cm to the southwest. Similarly, the lower hemisphere is moved approximately 30 cm. The vertical displacement at the western edge uplifts about 11 cm, and the eastern part uplifts about 8 cm (Fig. 8). Then, the spherical shape was squashed diagonally. The difference in displacement between the western and eastern hemispheres gives the expansion of the magma reservoir, but the estimated volume change was less than 1%. The possibility of triggering vesiculation by depressurization depends strongly on the state of magma, including factors like bubble density and viscosity (Papale and Polacci 1999; Hill and Prejean 2005; Walter and Amelung 2007). Therefore, we need a more quantitative model to evaluate this mechanism as a next step. Once vesiculation starts, this phenomenon accelerates with positive feedback (Fujita et al. 2013). The stress perturbation at the surface of a magma system is depicted in

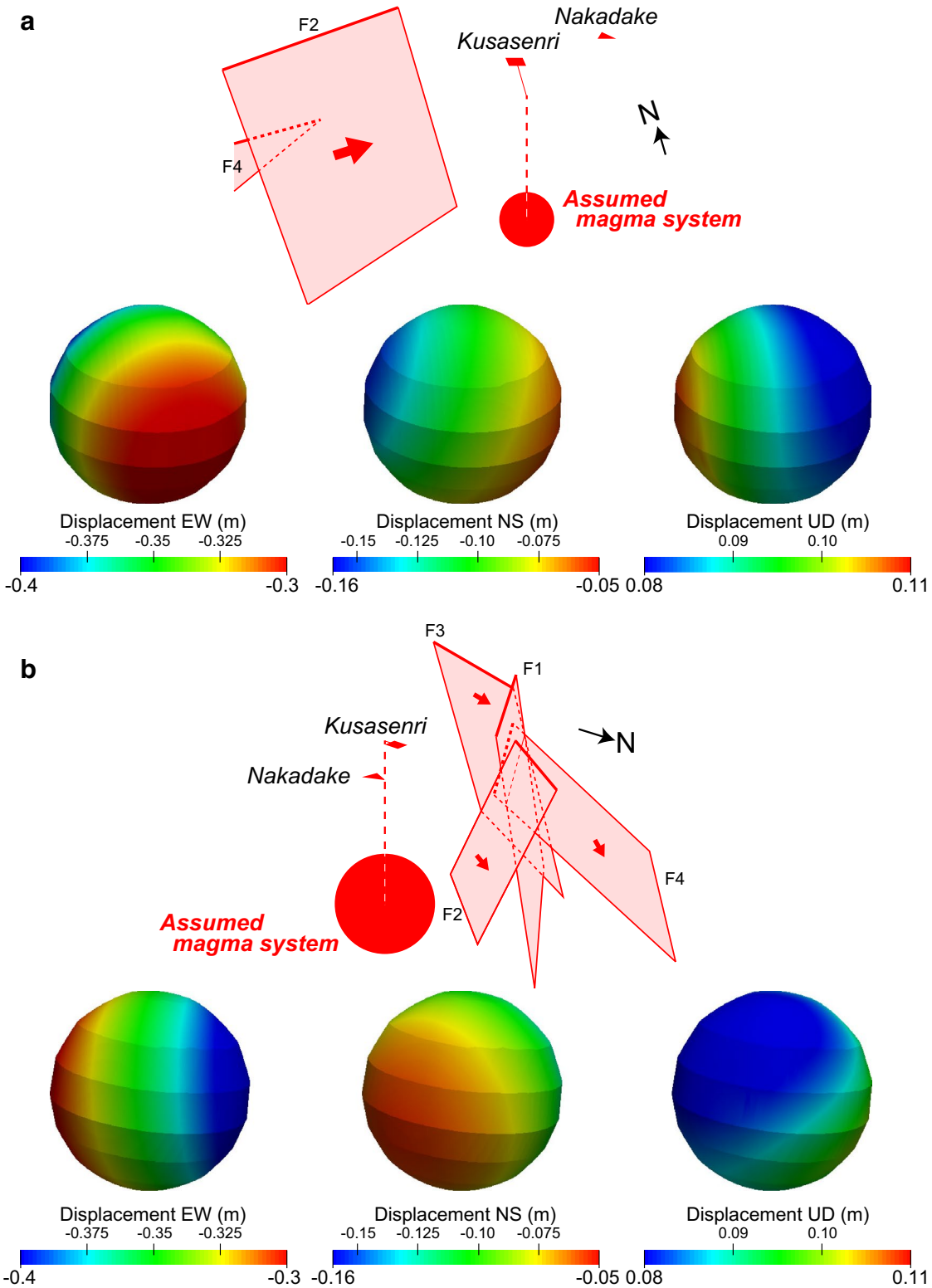

Fig. 8 Displacement distribution due to the 2016 Kumamoto Earthquake on the spherical surface of the Aso magma system. The magma system is assumed to be a 1-km-radius sphere 6 km beneath the area south of Kusasenri (Sudo et al. 2006). Displacements in the EW, NS and UD components are depicted as viewed from the southwest (**a**) and northeast (**b**), respectively. The *squares* indicate the seismic faults (F1, F2, F3, and F4) obtained from the SAR analysis in the previous section

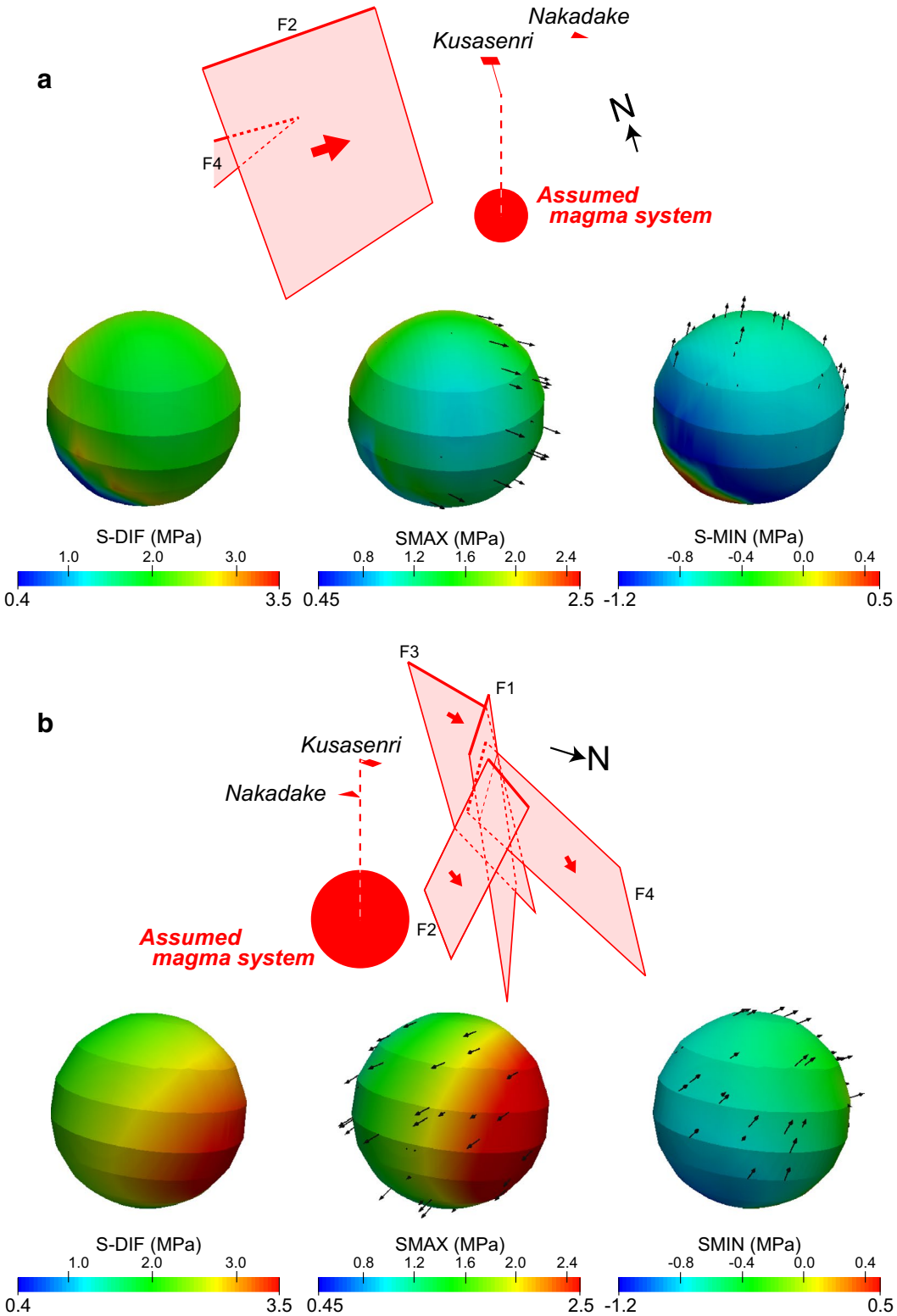

Fig. 9 Differential stress (S-DIF) and maximum (S-MAX) and minimum (S-MIN) principal stresses loaded on the surface of magma system by the movement of the seismic faults (F1, F2, F3, and F4) of the 2016 Kumamoto Earthquake, viewed from the southwest (**a**) and northeast (**d**). *Thin lines* indicate the axes of maximum and minimum principal stress, respectively

Fig. 9. It is noted that the uppermost northwestern part of the magma reservoir, the closest region to the F2 fault segment, is affected by a stress perturbation as large as 3.5 MPa in differential stress (S-DIF in Fig. 9). In contrast, the differential stress in the lower western hemisphere is approximately 0.4 MPa. The minimum principal stress in the northwestern part of the lower hemisphere indicates tensional stress change about 1.2 MPa. The axes of maximum and minimum stress are dipping toward south-southeast and west-northwest, respectively.

The deformation of a magma reservoir is definitely determined by the geometrical setting between the magma system and a seismic fault. First, the distance from the fault to the magma reservoir (R) is the most effective factor, since the stress change is inversely proportional to R^3. In this calculation, the magma reservoir is located in the neighborhood of the F2 fault segment and generates a complex distribution on the surface of the magma system. Some portions experience contraction and other parts are expanded by tensional stress. In Figs. 8 and 9, we model the magma reservoir beneath the area south of the Kusasenri region as inferred from Sudo et al. (2006). In addition, we check the sensitivity at the location, assuming the presence of other magma reservoirs beneath the Nakadake crater (Fig. 10). If the magma system is located apart from the F2 fault segment, the displacement and differential stress becomes smaller. In the case that the magma system is located beneath Nakadake, the stress perturbation was estimated to be approximately 1.8 MPa (Fig. 10). Although this is only about 51% of the perturbation in the magma system beneath the area south of the Kusasenri region, it is still large. Stress changes on the order of megapascals are sufficient to open a pre-existing crack and cause active magma migration (Walter 2007).

Confidence of the estimated fault model

In this section, we discuss about confidence of the estimated fault model. The F1 segment corresponds to the Futagawa Fault. As mentioned before, the decorrelation line was obtained along the Futagawa Fault, and the strike direction and the upper margin of the F1 segment are obvious from its feature. The rake angle of the fault slip was estimated to 203°, and it is consistent with the right-lateral offset of the Futagawa Fault revealed from geological surveys (e.g., Watanabe et al. 1979). Figure 11a shows the relation between the location of the F1 segment and the aftershock distribution. Seismicity around the segment is low, and that in the deeper extension is high. Generally, high seismicity area often appears in the surrounding area of the significant rupture by stress redistribution. Considering such a relation, the configuration of the F1 segment is consistent with aftershock distribution, and it is reasonable that the segment has a high dip angle.

The F2 segment corresponds to the northeast extension of the Futagawa Fault and is close to the magma system assumed in this study (the distance is approximately 3 km). According to the active fault map, the Futagawa Fault terminates at the west margin of the Aso caldera, and the active fault has not been mapped in the caldera. Seismicity around this segment has been very low, and thus it is difficult to verify its configuration from the seismic data such as the aftershock distribution and focal mechanisms. However, the strike direction and the location of the upper margin are obvious from high gradient of crustal deformation, and then validity of the dip angle is important for the F2 segment. We investigated residual distributions for tentative fault models in cases that the F2 segment had different dip angles, 40° (lower dip angle), 90° (higher dip angle), and 110° (the segment dips to the opposite side). Here, we estimated the fault models fixing a dip angle, and the initial parameters in this estimation were those for the best-fit model. Figure 12 shows the comparison of residuals of the observed and simulated crustal deformations. Obvious larger residuals were found around the F2 segment for all tentative fault models. Therefore, it is plausible that the F2 segment dips to southeast with high dip angle.

The F3 segment corresponds to the Hinagu Fault. As mentioned before, high gradient line of crustal deformation was obtained alongside the Hinagu Fault, and the strike direction and the location of the upper margin are obvious from its feature. The rake angle of the fault slip was estimated to 180°, and it is consistent with the right-lateral offset of the Hinagu Fault revealed from geological investigations (e.g., Chida 1979). According to the F-net catalogue, the strike-slip type focal mechanism was dominant around the F3 segment, and strike directions for $M_{JMA}5$ earthquakes were N211°E–N216°E, corresponding to that of the F3 segment. Dip angles were 74°–89°, and it roughly corresponds to that of the F3 segment. Figure 11b shows the relation between the location of the F3 segment and the aftershock distribution. Seismicity is low around the upper- and mid-parts of the segment, and that is high around the bottom part. However, it seems that the location of the F3 segment and the alignment line of aftershock distribution are slightly different. Additionally, high gradient line of crustal deformation was not consistent with the Hinagu Fault as mentioned before. It suggests that multiple fault segments may have been ruptured around this area. However, as a simple model for rough estimation of the effect on the magma system of the Aso volcano, this model must be acceptable.

The F4 segment is located alongside the east part of the Futagawa Fault and intersects the F1 segment at a

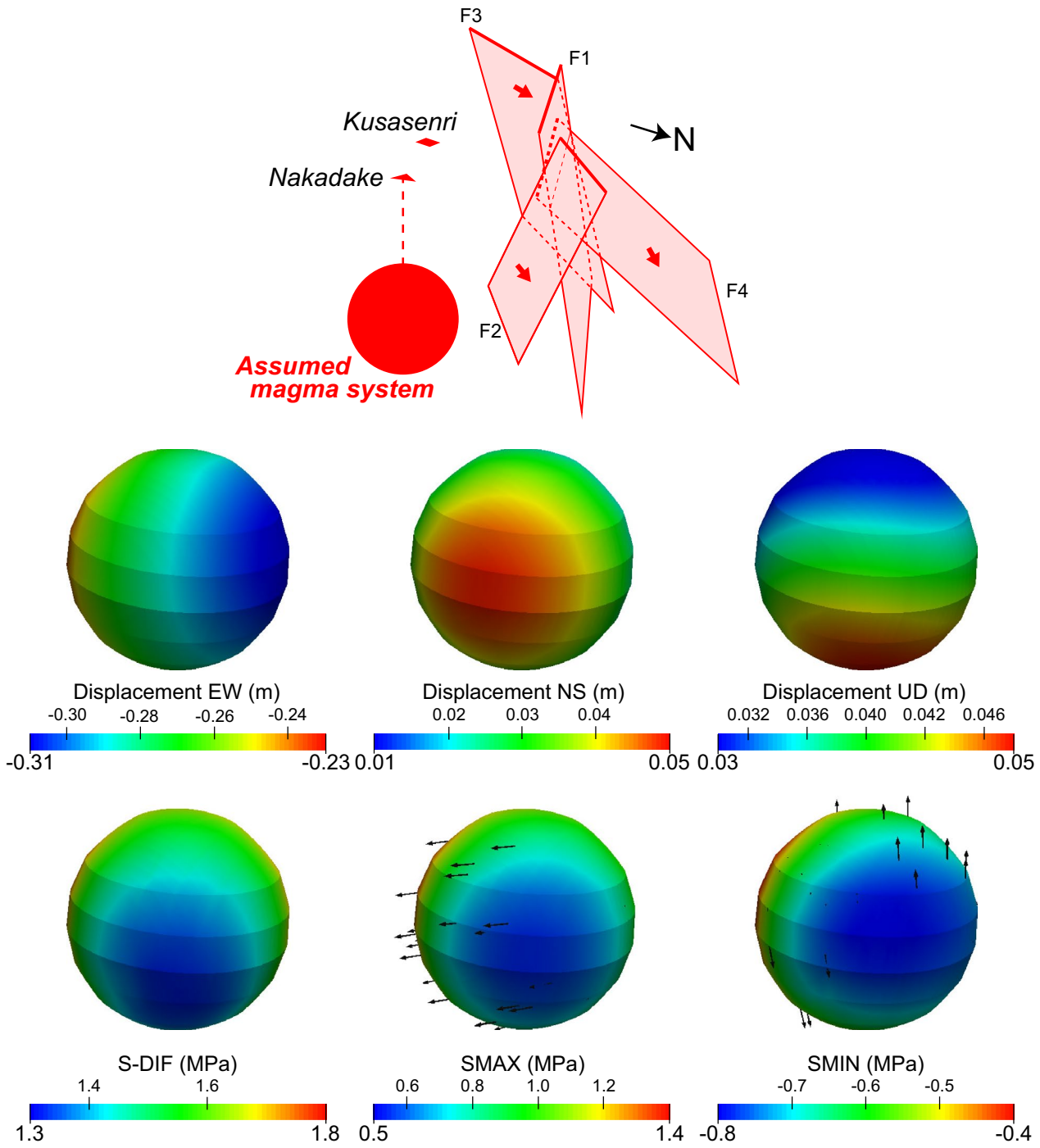

Fig. 10 Displacement (EW, NS, UD), differential stress (S-DIF), maximum principal stress (S-MAX), and minimum principal stress (S-MIN) distributions due to the 2016 Kumamoto Earthquake on the spherical surface of the Aso magma system. In this calculation, the magma system is assumed to be a 1-km-radius sphere 6 km beneath the Nakadake crater. The *squares* indicate the seismic faults (F1, F2, F3, and F4) obtained from the SAR analysis in the previous section. *Thin lines* indicate the axes of maximum and minimum principal stress, respectively

shallow depth. We assumed this segment for explaining crustal deformation obtained from InSAR pair 1 (Figs. 2, 4), slant-range extension which was obtained in both sides of the Futagawa Fault. The F4 segment has a low dip angle of 38°. The rake angle of the F4 segment was estimated to be 237° including large normal-slip component, though pure right-lateral slips were estimated for other segments. Around the F4

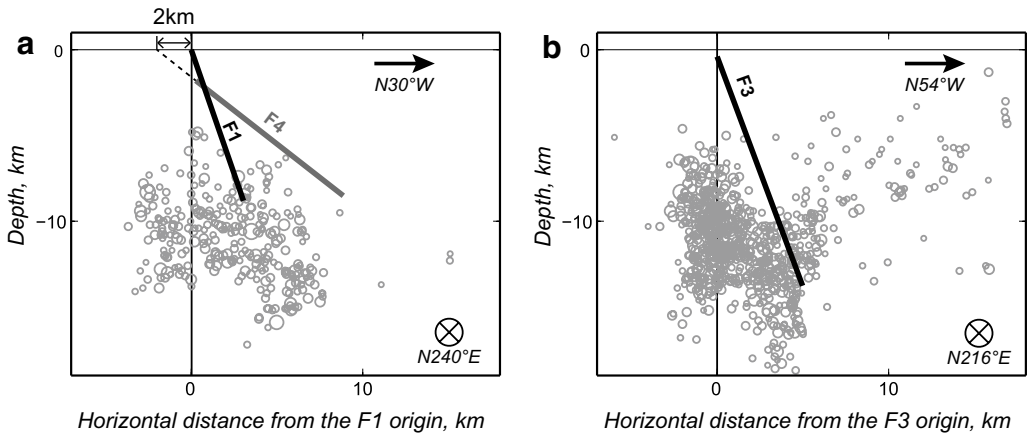

Fig. 11 Cross section of the distribution of aftershocks which occurred within the length of segment. **a** Cross section around the F1 segment. **b** Cross section around the F3 segment

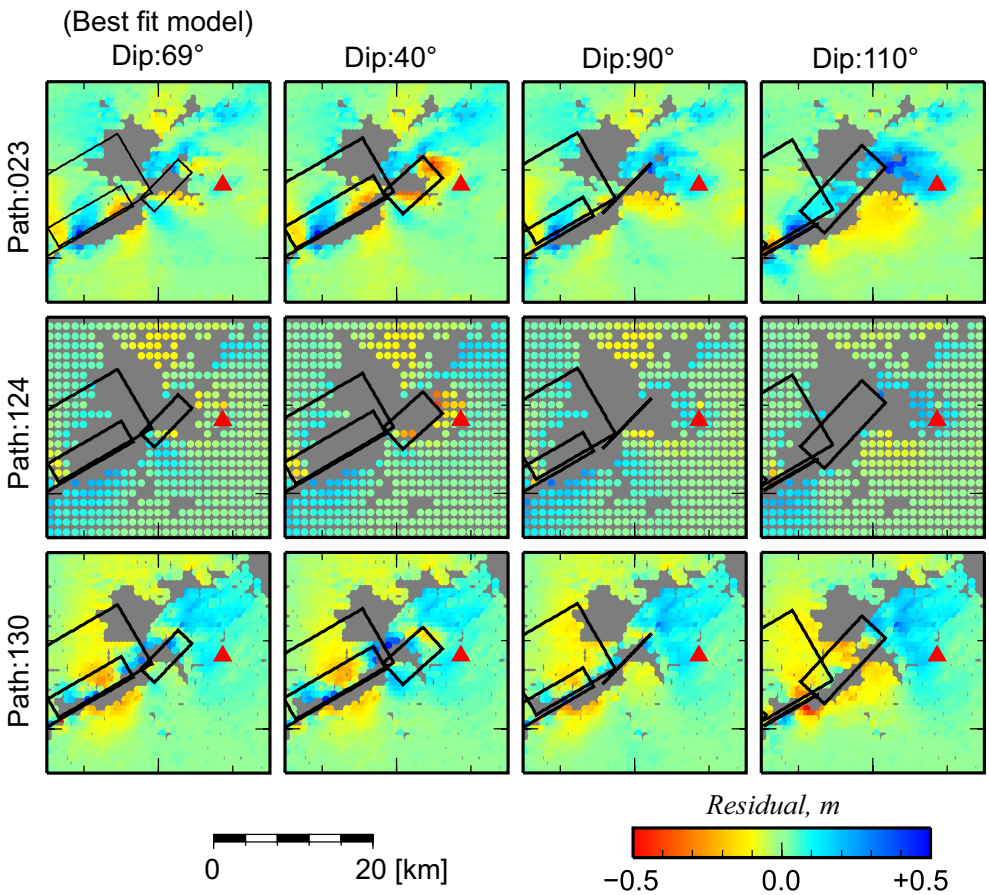

Fig. 12 Comparison of residuals between the observed and simulated crustal deformations

segment, several shallow aftershocks with a normal-slip mechanism occurred, and two earthquakes in them exceeded $M_{JMA}5$. Their strike directions were N238°E and N286°E, and dip angles were 35° and 38°, corresponding to that of the F4 segment. Furthermore, the shallower extension of the F4 segment is roughly

consistent with another parallel fault line of the Futagawa Fault.

Kubo et al. (2016) estimated source rupture process from strong motion waveforms, and large right-lateral slips were obtained near the F1–F4 segments. Its amount was 2 m or larger, roughly corresponding to our model. In particular, fault slips around the F1, F2, and F3 segments were large. Furthermore, large normal-slip component was estimated around the F4 segment. Such features are consistent with those of the fault model in this study.

As mentioned above, the estimated fault model is mostly consistent with results from seismic observation data and geological surveys. Then, we think that the estimated fault model must be acceptable for estimating the effect of crustal deformation on the magma system of the Aso volcano. Although we aimed at estimating the simple fault model in this study, a more accurate fault model could be estimated by considering the heterogeneity of the fault slip distribution. It is one of the issues for future research.

Summary

We detected crustal deformation associated with the 2016 Kumamoto Earthquake using InSAR and GNSS and found a decorrelation line and a steep gradient line of slant-range change along the Futagawa Fault, along the northeast extension of the Futagawa Fault, and alongside the Hinagu Fault. Additionally, we found a complex fringe pattern west of the Aso caldera, suggesting that shallow fault slips occurred in many known and unknown faults associated with the earthquake. Most of the crustal deformation could be explained reasonably by four rectangle faults located along the Futagawa Fault (F1), in the northeast extension of the Futagawa fault (F2), alongside the Hinagu Fault (F3), and in the eastern part of the Futagawa Fault (F4). The first-mentioned three faults have high dip angles and right-lateral slip, and the last fault has a low dip angle and normal-dip right-lateral slip. The estimated fault model is consistent with the aftershock distribution and seismic mechanisms.

Based on the estimated fault model, we estimated the effect of crustal deformation on the Aso magma system using FEM. Our calculation suggests the following two points. (1) Deformation and stress perturbations were very complicated, since the assumed location of the magma system was close to a seismic fault, especially the F2 fault segment. In general, the spherical magma system deformed slightly to an ellipsoid, and the total volume increased. In this case, the magma in the reservoir can be depressurized, and this may lead to degassing from the magma. (2) The differential stress around the northeastern portion of the magma system was as large as 3.5 MPa. It is on the order of stress disturbances that could trigger an opening of a pre-existing fracture around the magma reservoir and the intrusion of magma.

We are monitoring volcanic activity using V-net observation, and no obvious increase or decrease in activity has been observed through the time of this paper submission (September 2016). However, we have shown that this earthquake could have effected the shape of the magma reservoir and local stress field, thereby possibly triggering processes that lead to enhanced volcanic activity. Hence, more detailed monitoring of the Aso volcano is important.

Additional file

Additional file 1. Interferograms obtained from InSAR pairs listed in Table 1. (a)–(f) were generated from InSAR pair of No. 1–6 listed in Table 1. *Solid curves* indicate active faults cataloged in the digital map of active faults (Nakata and Imaizumi 2002). A red triangle indicates the location of the Nakadake crater.

Authors' contributions

TO performed InSAR analysis and fault modeling. He also wrote the manuscript. EF modeled the crustal structure and magma system using FEM and calculated the displacement and stress fields caused by the earthquake. HO performed GNSS analysis. All authors read and approved the final manuscript.

Acknowledgments

We are grateful to two anonymous reviewers and Prof. Nishimura for their valuable comments. We analyzed ALOS-2/PALSAR-2 data that are shared within the PALSAR Interferometry Consortium to Study our Evolving Land Surface (PIXEL) in this study. The data were provided by the Japan Aerospace Exploration Agency (JAXA) under a cooperative research contract with the Earthquake Research Institute (ERI) at the University of Tokyo. This study was supported in part by the ERI cooperative research program. PALSAR-2 observations after the earthquake were carried out based on the Earthquake Working Group, a special project for evaluating ALOS for disaster mitigation, coordinated by the Geospatial Information Authority of Japan (GSI) and JAXA. The original PALSAR-2 data are owned by JAXA. GEONET data and the 10-m-mesh DEM published by GSI were used in this study. We used the unified hypocenter catalog processed in collaboration with the Japan Meteorological Agency (JMA) and the Ministry of Education, Culture, Sports, Science and Technology (MEXT). We used the Generic Mapping Tools (Wessel and Smith 1998) for drawing the figures.

Competing interests

The authors declare that they have no competing interests.

Received: 22 June 2016 Accepted: 5 November 2016
Published online: 22 November 2016

References

Aoki K (2008) Revised age and distribution of ca. 87 ka Aso4 tephra based on new evidence from the northwest Pacific Ocean. Quatern Int 178:100–118. doi:10.1016/j.quaint.2007.02.005

Bautisa BC, Leonila PB, Stein RS, Barcelona ES, Punongbayan RS, Laguerta EP, Rasdas AR, Ambubuyog G, Amin EQ (1996) Relationship of regional and local structures to Mount Pinatubo activity. In: Newhall C, Punongbayan RS (eds) Fire and Mud. University of Washington Press, Seattle, pp 351–370

Birch F (1961) The velocity of compressional wave in rocks to 10 kilo bars (part II). J Geophys Res 61:1083–1102. doi:10.1029/JZ066i007p02199

Chida N (1979) Late quaternary activity of Hinagu fault, West Central Kyushu, annals of the Tohoku Geographical Association, vol 31, pp 172–179
Ebmeier SK, Elliot JR, Nocquet J-M, Biggs J, Mothes P, Jarrín P, Yépez M, Aguaiza S, Lundgren P (2016) Shallow earthquake inhibits near Chiles-Cerro Negro volcanoes, Ecuador-Colombian border. Earth Planet Sci Lett 450:283–291. doi:10.1016/j.epsl.2016.06.046
Fujita E, Kozono T, Ueda H, Kohno Y, Yoshioka S, Toda N, Kikuchi A, Ida Y (2013) Stress field change around the Mount Fuji volcano magma system caused by the Tohoku megathrust earthquake, Japan. Bull Volcanol 75:679. doi:10.1007/s00445-012-0679-9
Hill DP, Prejean S (2005) Magmatic unrest beneath Mammoth Mountain, California. J Volcanol Geotherm Res 146:257–283. doi:10.1016/j.jvolgeores.2005.03.002
Kubo H, Suzuki W, Aoi S, Sekiguchi H (2016) Source rupture processes of the 2016 Kumamoto, Japan, earthquakes estimated from strong motion waveforms. Earth Planets Space 68:161. doi:10.1186/s40623-016-0536-8
Lara LE, Naranjo JA, Moreno H (2004) Rhyodacitic fissure eruption in Southern Andes (Cordon Caulle: 40.5 S) after the 1960 (Mw: 0.5) Chilean earthquake: a structural interpretation. J Volcanol. Geotherm. Res. 138:127–138. doi:10.1016/j.jvolgeores.2004.06.009
Lemoine FG, Smith D, Smith R, Kunz L, Pavlis E, Pavlis N, Klosko S, Chinn M, Torrence M, Williamson R, Cox C, Rachlin K, Wang Y, Kenyon S, Salman R, Trimmer R, Rapp R, Nerem S (1997) The development of the NASA GSFC and NIMA joint Geopotential model. In: Segawa J et al (eds) IAG Symposium of gravity, geoid, and marine geodesy, vol 117. Springer, New York, pp 461–469
Manga M, Broadsky EE (2006) Seismic triggering of eruptions in the far field: volcanoes and geysers. Annu Rev Earth Planet Sci 34:263–291. doi:10.1146/annurev.earth.34.031405.125125
Marquardt DW (1963) An algorithm for least-squares estimation of non-linear parameters. J Soc Indust Apll Math 11(2):431–441. doi:10.1137/0111030
Matsubara M, Obara K, Kasahara K (2008) Three-dimensional P- and S-wave velocity structures beneath the Japan Islands obtained by high-density seismic stations by seismic tomography. Tectonophysics 454:86–103. doi:10.1016/j.tecto.2008.04.016
Matsumoto A (1996) K–Ar age determinations of young volcanic rocks -correction for initial 40Ar/39Ar ratios and its application. Chishitsu News 501:12–17 **(in Japanese)**
Nakata T, Imaizumi T (eds) (2002) Digital active fault map of Japan. University of Tokyo Press, Tokyo (in Japanese)
Okada Y (1985) Surface deformation due to shear and tensile faults in a half-space. Bull Seism Soc Am 75:1135–1154
Okada Y, Kasahara K, Hori S, Obara K, Sekiguchi S, Fujiwara H, Yamamoto A (2004) Recent progress of seismic observation networks in Japan Hi-net, F-net, K-NET and KiK-net. Earth Planets Space 56:XV–XXViii. doi:10.1186/BF03353076
Ono K, Watanabe K (1985) Geological map of aso volcano. geological map of volcanoes, Geological Survey of Japan, 4 (in Japanese with English abstract)
Ozawa T, Fujita E (2013) Local deformations around volcanoes associated with the 2011 off the Pacific coast of Tohoku earthquake. J Geophys Res 118:390–405. doi:10.1029/2011JB009129
Ozawa T, Shimizu S (2010) Atmospheric noise reduction in InSAR analysis using numerical weather model. J Geod Soc Jpn 56:137–147. doi:10.11366/sokuchi.56.137 **(in Japanese with English abstract)**
Papale P, Polacci M (1999) Role of carbon dioxide in the dynamics of magma ascent in explosive eruptions. Bull Volcanol 60:583–594. doi:10.1007/s004450050253
Pritchard ME, Jay JA, Aron F, Henderson ST, Lara LE (2013) Subsidence at southern Andes volcanoes induced by the 2010 Maule, Chile earthquake. Nat Geosci 6:632–636. doi:10.1038/ngeo1855
Sandwell DT, Price EJ (1998) Phase gradient approach to stacking interferograms. J Geophys Res 103:30183–30204. doi:10.1029/1998JB900008
Sudo Y, Kong LSL (2001) Three-dimensional seismic velocity structure beneath Aso Volcano, Kyushu, Japan. Bull Volcanol 63:326–344. doi:10.1007/s004450100145
Sudo Y, Tsutsui T, Nakaboh M, Yoshikawa M, Yoshikawa S, Inoue H (2006) Ground deformation and magma reservoir at Aso Volcano: Location of deflation source derived from long-term geodetic surveys. Bull. Volcanol. Soc. Jpn. (Kazan) 51:291–309 **(in Japanese with English abstract)**
Takada Y, Fukushima Y (2013) Volcanic subsidence triggered by the 2011 Tohoku earthquake in Japan. Nat Geosci 6:637–641. doi:10.1038/ngeo1857
Ueda H, Kozono T, Fujita E, Kohno Y, Nagai M, Miyagi Y, Tanada T (2013) Crustal deformation associated with the 2011 Shinmoe-dake eruption as observed by tiltmeters and GPS. Earth Planets Space 65:517–525. doi:10.5047/eps.2013.03.001
Walter TR (2007) How a tectonic earthquake may wake up volcanoes: Stress transfer during the 1996 earthquake-eruption sequence at the Karymsky Volcanic Group, Kamchatka. Earth Planet Sci. Lett. 264:347–359. doi:10.1016/j.epsl.2007.09.006
Walter TR, Amelung F (2007) Volcanic eruptions following M ≥ 9 megathrust earthquakes: implications for the Sumatra-Andaman volcanoes. Geology 35:539–542. doi:10.1130/G23429A.1
Watanabe K, Momikura Y, Tsuruta K (1979) Active faults and parasitic eruption centers on the west flank of Aso caldera, Japan. Quaternary Res 18:89–101. doi:10.4116/jaqua.18.89 **(in Japanese with English abstract)**
Wessel P, Smith WHF (1998) New improved version of generic mapping tolls released. EOS Trans AGU 79(47):579. doi:10.1029/98EO00426